Hong Ji, Yinlan Ruan, Heike Ebendorff-Heidepriem, Shahraam Afshar Vahid and Tanya Monro

A six-strut suspended core fiber for cylindrical vector mode generation and propagation

Optics Express, 2018; 26(24):32037-32047

DOI: http://dx.doi.org/10.1364/OE.26.032037

Research Article | Vol. 26, No. 24 | 26 Nov 2018 | OPTICS EXPRESS 32037
Optics EXPRESS

A six-strut suspended core fiber for cylindrical vector mode generation and propagation

HONG JI,[1,*] YINLAN RUAN,[1] HEIKE EBENDORFF-HEIDEPRIEM,[1] SHAHRAAM AFSHAR VAHID,[2] AND TANYA MONRO[1,2,3]

[1]*ARC Centre of Excellence for Nanoscale BioPhotonics, Institute of Photonics and Advanced Sensing, School of Physical Sciences, the University of Adelaide, Adelaide, SA 5005, Australia*
[2]*Laser Physics and Photonic Devices Laboratories, School of Engineering, University of South Australia, Adelaide, SA 5001, Australia*
[3]*Tanya.Monro@unisa.edu.au*
[*]*Hong.Ji@adelaide.edu.au*

Abstract: We report fabrication and simulation of an F2 glass six-strut suspended core fiber (SCF) with small effective core diameter of 2.5 μm for cylindrical vector (CV) modes generation and propagation. Simulation results show that the fiber has a large effective refractive index difference in the order of 10^{-4}-10^{-3} between the first higher-order CV modes, including TE_{01}, $HE_{21}^{even\ and\ odd}$ and TM_{01} modes. TE_{01} and TM_{01} were experimentally generated and were evaluated as having high purity of 82 percent and 85 percent, respectively. The results demonstrate that the SCF is a competitive waveguide candidate for selectable CV mode generation and propagation.

1. Introduction

The cylindrical vector (CV) beams and orbital angular momentum (OAM) beams, characterized by a dark hollow center, have special properties with phase or polarization singularities. Typically for these beams, radially polarized light under tight focusing conditions has strong longitudinal electric field at the focus, while the azimuthally polarized light produces strong longitudinal magnetic field with zero electric field at the center of the focused beam [1]. Those properties have been explored for a variety of applications, such as far field nano/microscopy [2–6], trapping and acceleration of particles [7,8], material processing [9–11], laser machining [10], quantum optics [12] and high power lasers [13,14].

In recent years, optical fibers as a means of generating and propagating CV and OAM beams are gaining attention. Much progress has been made on designs of optical fibers supporting CV modes, which includes TE_{01}, HE_{21} and TM_{01} modes [15–20]. Doughnut-shaped radially and azimuthally polarized modes generated in fibers underpinned the demonstration of high power fiber lasers with reduced nonlinear and damage effects [21,22], and enabled applications for digital signal processing multimode communications [23]. Moreover, azimuthally polarized TE_{01} modes have been exploited in fiber based two photon endoscopy for nanoscale resolution imaging [24] and sensing [25]. The hybrid HE_{21} mode in fiber has been studied for fiber based stimulated emission depletion (STED) nano/microscopy [26,27]. All these fiber-based applications require a fiber that is capable of generating and propagating distinct, pure CV modes.

STED microscopy is a powerful far-field imaging technique that can achieve resolution beyond the diffraction limit [3,28]. It uses a Gaussian beam to excite the fluorophore and a red-shifted, doughnut-shaped beam spatially overlapped with the Gaussian beam to deplete the fluorescence spherically except at the dark center of the depletion beam. The resolution of STED microscopy is critically dependent on the dark center intensity of the doughnut

#346454 https://doi.org/10.1364/OE.26.032037
Journal © 2018 Received 20 Sep 2018; revised 26 Oct 2018; accepted 9 Nov 2018; published 19 Nov 2018

Optics EXPRESS

depletion beam, called the STED beam, since any residual light or misalignment of the dark central region directly degrades the depletion effect that yields nanoscale resolution.

Free space STED systems have a number of practical challenges associated with the high precision alignment required for the Gaussian beam and the STED beam. The conventional system setup is bulky, requiring a number of discrete optical components, and is susceptible to environmental thermal variations and vibrations which currently limit the application in clinical environments. One effective solution to address the alignment issue is to use a STED fiber to stably deliver the STED beam (comprising the fiber TE_{01} or HE_{21} Eigen-mode) and Gaussian beam of different wavelengths simultaneously through a single strand of fiber [20,24,26]. In addition to supporting two wavelengths beams, stable delivery along one fiber enables highly precise alignment and increases the STED system flexibility for applications, including making remote on-site imaging possible.

In most conventional fibers, the required fiber modes are normally degenerate with neighboring modes due to the fiber modes having nearly identical mode propagation constants. Fibers that have large mode propagation constants differences (i.e. large effective index differences) are required to deliver stable, pure CV modes for fiber-based STED microscopy. Fibers with specially designed glass claddings [24,26] have large core/cladding index contrast and hence large effective index differences. They were demonstrated to support CV modes propagation for STED application.

In this work, we report for the first time the successful fabrication of a six-strut suspended core fiber (SCF) using extrusion technique and experimental confirmation of stable fiber CV modes generation and propagation in the fiber. The fiber has a distinct structure with air cladding and hence significant larger core/cladding index contrast compared to those fibers with specially designed glass claddings. The strut number of six is selected because the core of a six-strut SCF has a hexagonal shape, which is closer to a circular core shape and hence results in more uniform, close to circular first higher order modes field distributions compared to that of SCFs with smaller number of struts. The fiber exhibits a loss of 1.5 dB/m at wavelength of 808 nm. Our fiber's first higher order modes, including azimuthally polarized TE_{01} mode, hybrid $HE_{21}^{\text{even and odd}}$ modes and radially polarized TM_{01} mode, have been theoretically investigated using finite element software COMSOL. The simulations show that our six-strut SCF with 2.5 μm effective core diameter is capable of generating and delivering stable CV modes such as TE_{01}, HE_{21} or TM_{01} modes individually with large effective refractive index difference between them in the order of 10^{-4}-10^{-3} which is about one order magnitude higher than that of fiber being reported so far. Using the measured field distribution of the TE_{01} mode, the maximum extinction ratio of this CV mode doughnut rim maximum field intensity to the dark center minimum field intensity was determined to be 5.6 dB. The purity of the experimentally generated TE_{01} and TM_{01} modes was found to be 82% and 85%, respectively.

2. Fiber fabrication and characterization

In this work, a commercially available lead silicate F2 glass (Schott Glass Co.) was used. F2 glass is attractive because it combines high transmission in the visible spectral range with a low softening temperature of 592°C [29]. The high transmission in the visible is of interest for (bio) chemical sensing and imaging applications since it allows for the efficient excitation of a range of fluorophores (for examples, quantum dot labelled proteins at 532 nm [30], nano diamonds of type IIa [31] at 532 nm or xanthene dye JA26 at 635 nm [32]). The low softening temperature makes it possible to extrude the glass through stainless steel dies for preform and jacket tube fabrication [33]. The refractive index of F2 glass (n = 1.62 at 588 nm) is higher than that of silica glass (n = 1.46 at 588 nm) bringing advantages such as higher sensitivity due to enhanced fluorescence capture fraction [34], tighter mode confinement and higher optical nonlinearity.

Optics EXPRESS

The fibers were made in a three-step process using the extrusion technique for preform fabrication [33], which is a more reproducible and economical fabrication process than the stacking technique traditionally used to produce microstructured optical fibers. Firstly, the structured preform and jacket tube with outer diameter (OD) of ~12 mm and ~10 mm, respectively, were extruded from F2 glass billets of ~30 mm diameter. Secondly, the preform was reduced in size to a "cane" of ~1 mm OD using a fiber drawing tower. This cane was inserted into the jacket tube with inner diameter (ID) fitting closely to the cane. Finally, the assembly was drawn down to the final SCF with 125 μm OD.

The dimensions of the preform, cane and fiber features (OD, core diameter, strut length and thickness) were measured using cross-sectional images taken using a digital camera for the preform, an optical microscope for the cane and a scanning electron microscope (SEM) for the fiber. For the cane and fiber, the average dimensions of several samples were determined. The cross-section of the extruded structured preform is shown in Fig. 1(a). The structure comprises a central solid core supported by six long thin struts, which extend along the preform length. The cross-section of the drawn cane [Fig. 1(b)] shows that the structure has been well maintained during the scale-down draw process. As the SCF has a hexagonal core shape [Fig. 1(c)-1(e)], we define the fiber core diameter d as the diameter of the circle that is inscribed within the hexagonal core, whereas the effective core diameter d_{eff} is defined as the diameter of the circle that has the same area as the hexagon that fits wholly within the SCF core, i.e. $d_{eff} = 1.05 \times d$, as shown in Fig. 1(e). The SCF has OD of 125 μm and core diameter d of 2.36 μm ($d_{eff} = 2.5$ μm). The fiber core is suspended in the outer glass region by six fine struts with length s of ~3.9 μm and thickness of less than 150 nm. The outer glass region protects the small core and thin struts and provides sufficient mechanical strength for handling and cleaving the fiber. The air holes make up the cladding, with the fine struts suspending the core in the air cladding while being sufficiently thin and long to enable tight mode confinement.

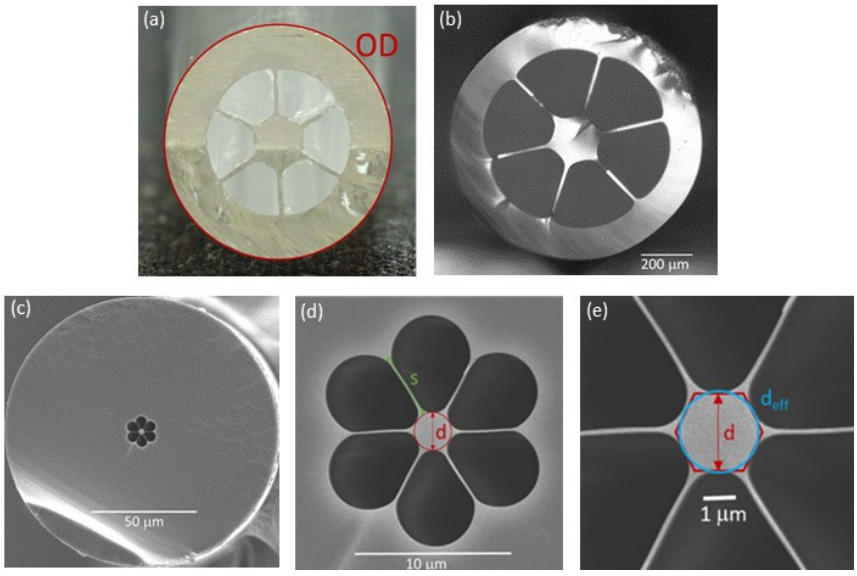

Fig. 1. Cross-sectional images and definitions of the cross-sectional structure features of (a) extruded preform taken by digital camera; (b) drawn cane taken by optical microscope; (c)-(e) drawn SCF taken by SEM.

In [29], modelling of the Gaussian confinement loss of F2 glass three-strut SCF shows that the air cladding to effective core radius ratio, r_{air}/r_{eff}, at 0.1 dB/m confinement loss decreases with increasing effective core diameter normalized to the wavelength λ, d_{eff}/λ, with the air cladding radius being defined as the sum of one strut length and effective core radius,

Optics EXPRESS

$r_{air} = s + r_{eff}$. In [29], for the largest modelled $d_{eff}/\lambda = 1$, the r_{air}/r_{eff} ratio is 3.5. Compare to our fiber, d_{eff}/λ is 3.1 and r_{air}/r_{eff} is 4.1. The similarity of the modelled r_{air}/r_{eff} for the three-strut SCF with the measured r_{air}/r_{eff} for our six-strut SCF suggests that the confinement loss of our fiber for Gaussian mode is ~0.1 dB/m. From the modeling of our F2 glass six-strut SCF, the confinement loss for TE_{01} mode is calculated to be ~0.4 dB/m for the mode at 808 nm wavelength which is also small. In addition, the absence of significant increase of the measured fiber loss for >808 nm wavelength as shown below indicates negligible confinement loss for our fiber up to 1.2 μm wavelength.

The fiber loss was measured using the cut-back loss measurement technique with a plasma white light source. The loss spectrum for the fiber is shown in Fig. 2. At the wavelength of 808 nm, considered here for STED microscopy, the fiber loss of ~1.5 dB/m for our six-strut SCF with d_{eff} = 2.5 μm core is slightly higher than the loss of ~0.6 dB/m for a three-strut F2 glass SCF with d_{eff} = 2.1 μm core [29,35]. Possible reasons for higher loss are fiber core surface contamination and different glass flow in the die used for our fiber compared to the die design used for the three-strut SCF. The loss of 1.5 dB/m is acceptable for applications requiring only a couple of meters of fiber, such as fiber-based STED microscopy for in-vivo bio-imaging over short distance in a clinical environment. In this work, we approximate the loss of each mode to be the same as overall fiber loss we measured which is based on a beam supposed comprising all modes.

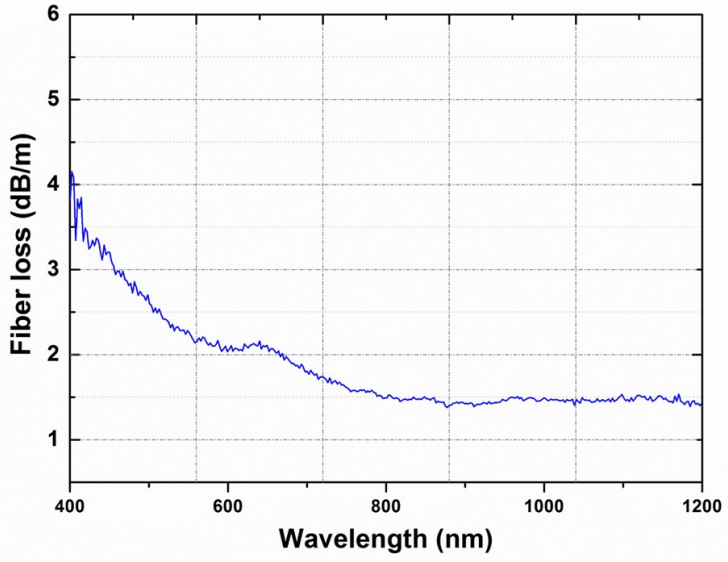

Fig. 2. Measured loss spectrum for the fabricated fiber.

3. Modeling of the first higher-order modes

Large mode propagation constant differences between a fiber's first higher order modes (typically with doughnut shape fields distributions that resemble CV beams) are essential to prevent degeneration or coupling between neighboring modes, enabling stable CV mode propagation along the fiber, which is critical for STED microscopy. To evaluate the propagation properties of the first higher order modes in our six-strut SCF, numerical modelling of those modes in the fiber were performed. To understand the impact of core shape and symmetry on mode field distribution, we modelled not only the fabricated, real six-strut fiber with asymmetric hexagonal core (using the vectorized geometry based on the tested real fiber cross-section SEM image) but also an ideal six-strut fiber with symmetric hexagonal core having the same effective core diameter of 2.5 μm as the real six-strut fiber (using constructed geometry) and an air-clad (unstructured) fiber with circular core having the

Optics EXPRESS

same diameter. These three fiber structures were modelled using refractive index of 1.6 at wavelength of 808 nm and commercially available finite element modelling software COMSOL [27].

The large core/cladding refractive index contrast of the fibers results in a large mode effective refractive index difference Δn_{eff} (hence large propagation constants difference) between the first higher order modes, which include TE_{01}, HE_{21} and TM_{01} modes. The simulation results of the field distribution of the TE_{01}, $HE_{21}^{odd\ and\ even}$ and TM_{01} modes for the three fiber structures investigated are shown in Fig. 3. For the real, asymmetric hexagonal core six-strut fiber, Δn_{eff} of the fundamental modes ($HE_{11}^{odd\ and\ even}$) and the first higher order hybrid modes ($HE_{21}^{odd\ and\ even}$) are in the order of 10^{-6}. Δn_{eff} between the TE_{01} and the neighboring first higher order HE_{21} mode and between TM_{01} and its neighboring HE_{21} mode are in the order of 10^{-3}. These index difference scales are expected to support stable TE_{01} and TM_{01} modes propagation along the fiber as these values are at least one order of magnitude higher than that reported for a fiber with specially design glass cladding (1.8×10^{-4}), which showed experimentally stable CV mode propagation [20].

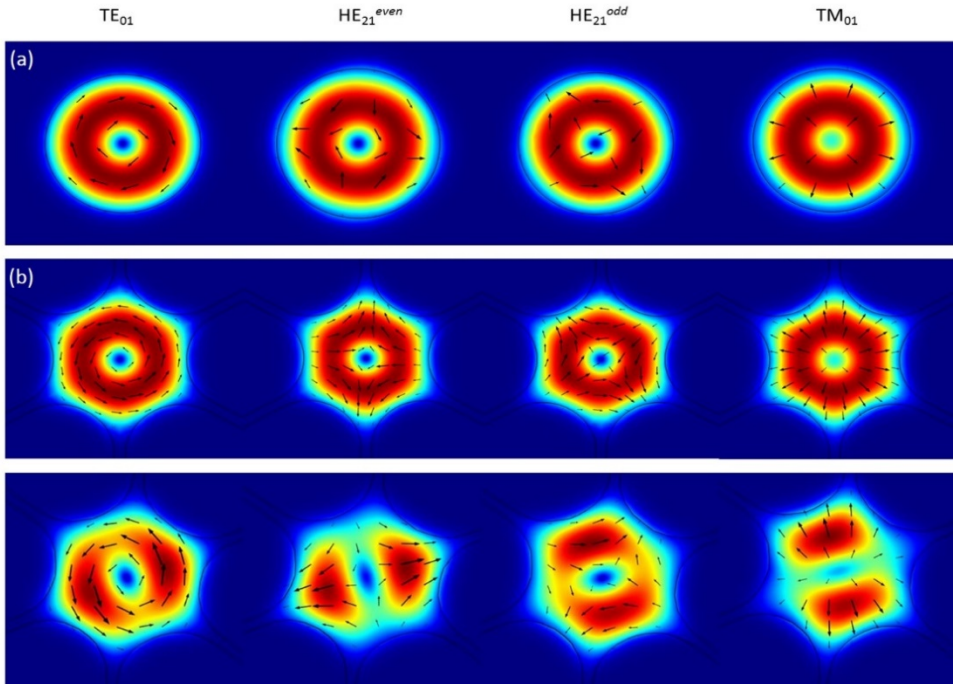

Fig. 3. The first higher order mode field distributions at 808 nm wavelength and 1.6 glass refractive index for (a) air-clad fiber with circular core of 2.5 μm diameter, (b) ideal six-strut fiber with symmetric hexagonal core of 2.5 μm effective diameter, (c) real six-strut fiber with asymmetric hexagonal core of 2.5 μm effective diameter.

The first higher order Eigen-mode fields of the CV modes of the circular core air-clad fiber and the ideal symmetric hexagonal core six-strut fiber are distributed symmetrically in doughnut shapes in the fibers' cross section [Figs. 3(a) and 3(b)]. The circular core air-clad fiber has doughnut modes with circular outer and circular inner shape, while the symmetric hexagonal core six-strut fiber has doughnut modes with hexagonal outer and circular inner shape. Comparison of the mode field distributions of the circular core and symmetric hexagonal core fibers shows that both fibers have identical field polarizations. By contrast, the real, asymmetric hexagonal core six-strut fiber which has been modelled for the first time in this work has shown distorted mode field distribution [Fig. 3(c)] due to the asymmetric

Optics EXPRESS

geometry of the core in the fabricated SCF. The effect of the distortions will be reported in detail in future work.

The refractive index differences between the CV modes for the three fiber structures investigated at 808 nm wavelength are listed in Table 1. More detailed Δn_{eff} properties of the ideal symmetric core six-strut SCF were reported in [27] which focused on theoretical modeling of SCFs with different materials and dimensions to understand the properties of the fiber. For the circular core air-clad fiber, Δn_{eff} between the TE_{01} or TM_{01} and the neighboring HE_{21} modes is in the order of 10^{-3}. Both the symmetric and the asymmetric hexagonal core six-strut fibers have similar Δn_{eff} values, which are approximately half of the circular core air-clad fiber. The results show that our real SCF has a high Δn_{eff} of 1.427×10^{-3} between TE_{01} and the neighboring HE_{21} which is in the same order as that of circular core air-cladding fiber. Although Δn_{eff} between TM_{01} mode and the neighboring HE_{21}^{odd} mode in the symmetric and asymmetric hexagonal core six-strut fibers (8.22×10^{-4} and 9.25×10^{-4}, respectively) is smaller than that in the circular core air-clad fiber (1.723×10^{-3}), these Δn_{eff} are well in line with the mode stability proxy $\Delta n_{eff} > 10^{-4}$ [19,36] to support distinct mode generation and propagation. The hybrid modes have Δn_{eff} in the order of 10^{-6} for the circular core air-clad fiber and the ideal symmetric core SCF between the even and odd modes which is too small, making the propagation constants too close to make those modes distinguishable. For the real asymmetric core SCF, Δn_{eff} between the hybrid even and odd modes is calculated to be $\sim 7.232 \times 10^{-5}$ which is approaching the order of 10^{-4} and suggests a possible to be excited separately. According to the calculation, Δn_{eff} between the fundamental modes and the neighboring first higher order mode is 2.431×10^{-2} which is in the order of 10^{-2} to support the selective excitation of a fundamental mode in this fabricated SCF as well.

Table 1. Refractive index differences between the neighboring first higher order modes for circular core air-clad fiber, symmetric and asymmetric hexagonal core six-strut fibers.

fiber structure	$\Delta n_{eff}(TE_{01}\text{-}HE_{21}^{even})$	$\Delta n_{eff}(HE_{21}^{even}\text{-}HE_{21}^{odd})$	$\Delta n_{eff}(HE_{21}^{odd}\text{-}TM_{01})$
circular core air-clad fiber	2.41×10^{-3}	1.873×10^{-6}	1.723×10^{-3}
ideal symmetric core six-strut fiber	1.448×10^{-3}	8.408×10^{-6}	8.22×10^{-4}
real asymmetric core six-strut fiber	1.427×10^{-3}	7.232×10^{-5}	9.25×10^{-4}

4. Experimental results for CV mode field distributions in six-strut SCF

For the fabricated six-strut SCF with effective core diameter of 2.5 μm, TE_{01}, HE_{21} and TM_{01} modes have been successfully generated and investigated experimentally using the setup shown in Fig. 4. An S-waveplate (WOP: Workshop of Photonics), which is a super-structured space variant polarization converter, was used to convert a Gaussian beam into an azimuthally or radially polarized beam as the light source. A Gaussian beam from a pigtailed diode laser source with 808 nm wavelength (LOS_BLD_0808 2W, HTOE) is launched to a linear polarizer through a 40 × objective (0.65 NA) and propagated through the S-waveplate to convert the Gaussian beam to an azimuthally polarized doughnut beam or a radially polarized doughnut beam for TE_{01} mode and TM_{01} mode generation in the same fiber. With limited length of useful fabricated fiber, the length of the fabricated six-strut SCF for CV modes excitation testing varied from 30 cm to 80 cm. The fiber length was 43 cm for the best results reported in this work. The fiber was mounted on two NanoMax stages (Max313D/M, Thorlabs) placed closing to each other with the fiber bended with a bending radius of ~5 cm. The generated TE_{01} and TM_{01} modes from the output end of the fiber were measured by a CCD camera (LBA-FW-SCOR20, Spiricon) through a 60 × objective (0.75 NA). The modes' polarization characteristics were tested using a linear polarizer (LPNIR050, Thorlabs) set between the fiber output end and the CCD camera.

Optics EXPRESS

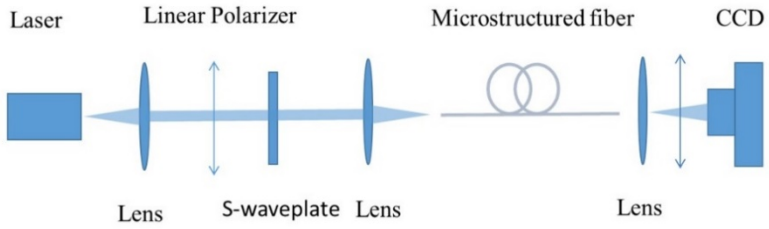

Fig. 4. Schematics of the experimental setup for CV modes generation in the six-strut SCF using input doughnut beam generated through an S-wave plate together with a linear polarizer.

In this setup, azimuthally and radially polarized free space beams are generated by the S-waveplate combined with the linear polarizer. When azimuthally polarized light is coupled into the SCF, a TE_{01} mode is generated and propagates along the fiber, while radially polarized light excites a TM_{01} mode in the fiber. The measured intensity distributions for TE_{01}, TM_{01} and HE_{21} odd modes of the real six-strut fiber shown in Fig. 5 closely resemble the predicted intensity distributions shown in the insets in Fig. 5 column (1). The results show that the first higher order group modes TE_{01} and TM_{01} can be selectively generated in the SCF due to the large Δn_{eff} in order of 10^{-3}-10^{-4} between the neighboring modes. Partial HE_{21}^{odd} mode was observed due to it has a Δn_{eff} with its near neighbor HE_{21}^{even} mode in the order close to ~10^{-4}.

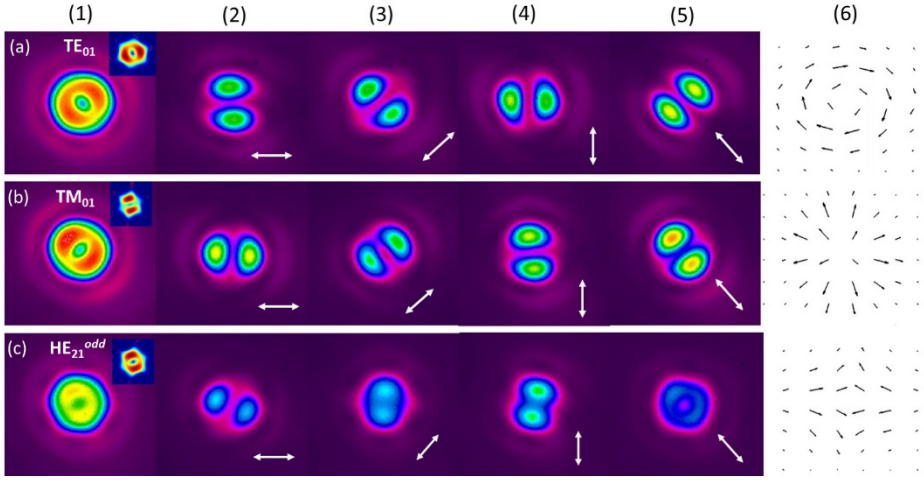

Fig. 5. (a)(1) Azimuthally polarized TE_{01} mode; (b) (1) radially polarized TM_{01} mode and (c)(1) hybrid polarized HE_{21} mode fields at λ of 808 nm obtained by imaging the near field at the end face of the fiber (fabricated six-strut SCF with effective core diameter of 2.5 μm) onto a CCD camera together with the linear polarizer in four orientations as indicated by the arrows in columns (2)-(5) and (6). Vector plots of the electric field orientations that were calculated from the measured horizontally and vertically polarized light intensity data. The insets in (a)(1), (b)(1) and(c)(1) are the calculated field distributions of the azimuthally polarized TE_{01}, radially polarized TM_{01} and hybrid HE_{21} modes of the fabricated SCF.

The intensity distributions measured with four different linear polarizer directions (as shown in Fig. 5 by the white arrows at 0 degree, 45 degree, 90 degree and 135 degree relative to horizontal direction) exhibit typically two lobes. The intensity distributions vary with linear polarizer. The orientation of the two lobes of the TE_{01} and TM_{01} modes turn in the same direction as the linear polarizer turning direction as shown in Fig. 5(a) and 5(b) columns (2)-(5), while the orientations of the two lobes of the HE_{21} mode turn in opposite direction to that of the linear polarizer turning direction as shown in Fig. 5(c) columns (2)-(5). By combining

Optics EXPRESS

the measured intensity at each point of the distributions of Fig. 5 columns (2) and (4), the local total intensity and the field orientations at any point in the cross section of the output beam can be calculated based on Stokes parameter S_0, which is the total intensity of the light according to [37]. The calculated output beam polarizations are shown in Fig. 5(a), 5(b) and 5(c) column (6).

The measured TE_{01} mode intensity distribution profile is shown in Fig. 6. The mode excitation efficiency was calculated. Using the ratio of the measured fiber output end power to the input end power, the TE_{01} mode total loss including TE_{01} mode coupling loss and the fiber transmission loss can be obtained. Subtracting the fiber transmission loss of the measured 1.5 dB/m, TE_{01} mode coupling efficiency is estimated to be ~8%. The TM_{01} mode and HE_{21}^{odd} mode excitation efficiencies were estimated to be ~21% and ~12%, respectively. The low coupling efficiency of the TE_{01} mode could be due to the fiber end cleaving issue and mismatching of the input beam size and the fiber core excited mode dimension etc. For a low coupling efficiency, a high power laser source would be required and such a source will increase the cost of the whole setup. The doughnut beam extinction ratio of the doughnut rim maximum field intensity to the central dark area minimum intensity was measured to be ~5.6 dB for the TE_{01} mode shown in Fig. 6 (corresponding to a residual intensity of ~28% of the maximum intensity of the doughnut rim in the dark center of the doughnut beam). This 28% residual intensity in the dark center for our six-strut SCF is much higher than the ~1% residual intensity in the dark center (18.75 dB extinction ratio) reported for a fiber with specially designed glass cladding [38]. The higher value of central dark area residual intensity for our fiber may come from various factors including the imperfection of the SCF core symmetry, wavelength mismatch between the S-wave plate (800 ± 25 nm) and laser line (808 ± 1 nm), imperfect laser beam quality, misalignment of the laser source beam center and S-waveplate center (limited by the components controlling precision of tuning position), imperfection of the S-waveplate and resulting imperfection of the doughnut beam source symmetry. The central dark area residual intensity of the STED beam spoils the STED image by drastically reducing the STED image intensity [39]. More specifically, for free space STED microscopy [39], 5% and 50% doughnut center intensity of the STED beam leads to an image with resolution of ~60 nm and ~160 nm, respectively, and 50% and 90% intensity drop, respectively, compared with a confocal image, which makes collection of a high quality image difficult. In our six-strut SCF, the central dark area intensity is ~28%, which is expected to result in a poor quality, dim STED image with >100 nm resolution. Hence optimization of our experimental setup and improvement of the fiber core symmetry are required to reduce the central dark area residual intensity.

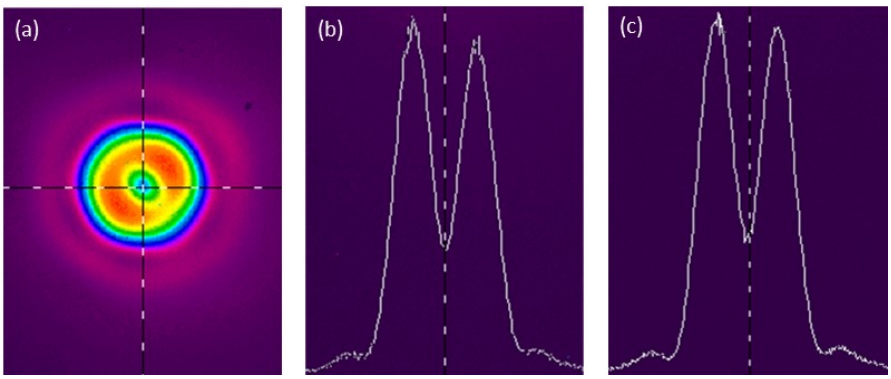

Fig. 6. TE_{01} mode (a) field distribution; (b) profile along horizontal dashed line and (c) profile along vertical dashed line.

For the azimuthally polarized TE_{01} mode, the orientation of the bisector of the two lobes is normal to the direction of the linear polarizer [Fig. 5(a) columns (2)-(5)]. For the field

Optics EXPRESS

distribution of this mode, the contour plot from the measured image is compared with the contour plot calculated using measured horizontally and vertically polarized components [Fig. 7 (a) and 7(b)]. Using the measured data of the output beam, the measured horizontally and vertically polarized fields together with the measured 74.5% linear polarizer transmission, the average TE_{01} mode purity (power of the azimuthally polarized component shown in Fig. 7(b) of the overall TE_{01} mode field intensity shown in Fig. 7(a)) was calculated to be 84%. Considering the linear polarizer transmission of 82.6% given in the polarizer data sheet, the purity was calculated to be 82%.

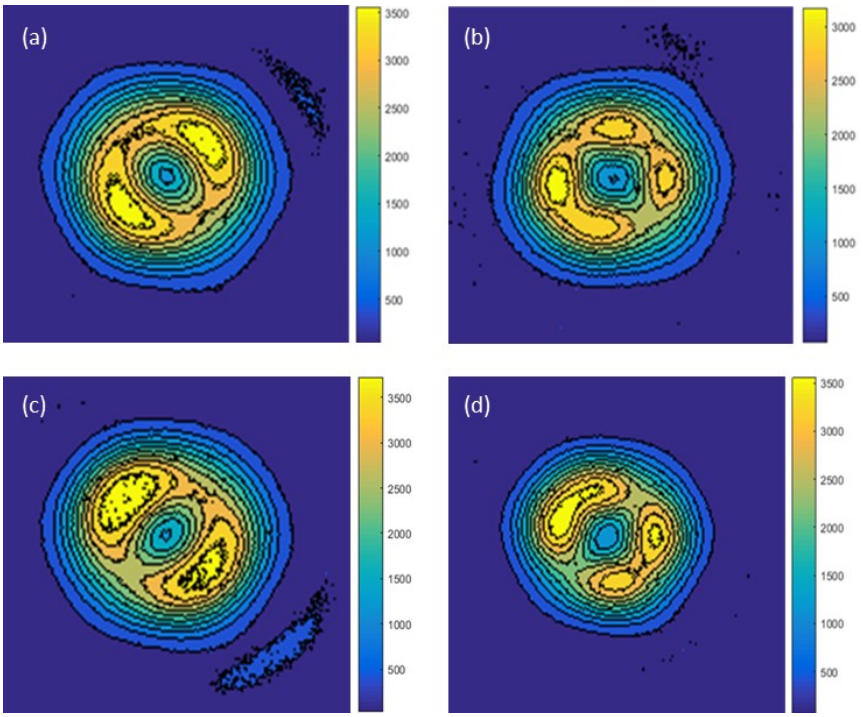

Fig. 7. Field intensity contour of (a) measured azimuthally polarized TE_{01} mode; (b) calculated azimuthally polarized TE_{01} mode using measured horizontally and vertically polarized distribution data; (c) measured radially polarized TM_{01} mode; (d) calculated radially polarized TM_{01} mode using measured horizontally and vertically polarized distribution data.

For the radially polarized TM_{01} mode, the orientation of the bisector of the two lobes is parallel to the direction of the linear polarizer [Fig. 5(b) columns (2)-(5)]. Using the measured polarizer transmission of 74.5%, the average TM_{01} mode purity was calculated to be as high as 90%. Using the 82.6% transmission listed in the polarizer datasheet, the mode purity was calculated to be higher as 85%. For both TE_{01} and TM_{01} modes, the calculated fields intensity distributions based on the horizontal and vertical polarization fields are more circular than the measured field intensity distribution based on CCD camera image.

For the hybrid HE_{21} mode, the orientation of the bisector of the two lobes is no longer orthogonal or parallel with the direction of the linear polarizer. The calculated local polarization is shown by the vector plot in Fig. 5(c) column (6). The calculated purity based on the data of the measured image is just 70%.

The same factors that contribute to the doughnut beam center intensity determine the purity of the measured higher order modes. Main factors include excitation beam and fiber core alignment error, input STED beam residual polarization errors and the fiber core geometry symmetry (especially for TM_{01} and HE_{21} modes in this experiment). The laser source and the detector noise introduced errors are negligible for the purity due to those

Optics EXPRESS

noises compared to the near saturated doughnut crest maximum intensities are small and also can be further cancelled out in the calculation. With high precision adjustment of the azimuthally or radially polarized input beam source position and distribution within the limitations of our experimental setup such as position tuning precision and S-waveplate quality, the alignment coupling error and beam source polarization error can be reduced. Using a fiber with higher core symmetry, the geometry induced mode field distribution distortion can be minimized.

5. Summary

We report for the first time in this work the real six-strut F2 SCF fabrication based on our previously modelling predictions and the experimental confirmation of the fiber's selective generation and propagation of individual TE_{01}, HE_{21} and TM_{01} modes with high purity. The fabricated high index F2 glass six-strut SCF provides significant high index contrast between glass core and air cladding and a small effective core size of 2.5 μm, enabling large effective index differences between the doughnut-shaped CV modes. Hence this structured SCF supports stable distinct mode generation and propagation. The experimental results show that stable TE_{01} and TM_{01} modes can be generated and propagated along our 43 cm long SCF with high purity of 82% and 85%, respectively. The mode purity can be further enhanced by improving alignment adjustment, input beam quality and fiber core symmetry. The TE_{01} mode in our SCF is of particular interest for fiber based STED micro/nano microscopy imaging.

Funding

T.M. Monro's Australian Research Council (ARC) Georgina Sweet Laureate Fellowship (FL130100044); ARC Centre of Excellence for Nanoscale Biophotonics (CE140100003).

Acknowledgement

This work was performed in part at the OptoFab node of the Australian National Fabrication Facility, utilizing Commonwealth and SA State Government funding. The authors thank Alastair Dowler at the University of Adelaide for his assistance in fiber fabrication, and also Stephen Christopher Warren-Smith, Mustaf Bekteshi, Roman Kostecki, Alexandre Francois, and Nicolas Riesen for technical assistance.

References

1. Q. Zhan and J. Leger, "Focus shaping using cylindrical vector beams," Opt. Express **10**(7), 324–331 (2002).
2. D. Wildanger, B. R. Patton, H. Schill, L. Marseglia, J. P. Hadden, S. Knauer, A. Schönle, J. G. Rarity, J. L. O'Brien, S. W. Hell, and J. M. Smith, "Solid immersion facilitates fluorescence microscopy with nanometer resolution and sub-ångström emitter localization," Adv. Mater. **24**(44), OP309–OP313 (2012).
3. S. W. Hell and J. Wichmann, "Breaking the diffraction resolution limit by stimulated emission: stimulated-emission-depletion fluorescence microscopy," Opt. Lett. **19**(11), 780–782 (1994).
4. T. Müller, C. Schumann, and A. Kraegeloh, "STED microscopy and its applications: new insights into cellular processes on the nanoscale," ChemPhysChem **13**(8), 1986–2000 (2012).
5. C. Eggeling, K. I. Willig, and F. J. Barrantes, "STED microscopy of living cells--new frontiers in membrane and neurobiology," J. Neurochem. **126**(2), 203–212 (2013).
6. K. I. Willig, B. Harke, R. Medda, and S. W. Hell, "STED microscopy with continuous wave beams," Nat. Methods **4**(11), 915–918 (2007).
7. Q. Zhan, "Trapping metallic Rayleigh particles with radial polarization," Opt. Express **12**(15), 3377–3382 (2004).
8. C. Varin and M. Piché, "Acceleration of ultra-relativistic electrons using high-intensity TM01 laser beams," Appl. Phys. B **74**(1), s83–s88 (2002).
9. L. Novotny, M. R. Beversluis, K. S. Youngworth, and T. G. Brown, "Longitudinal field modes probed by single molecules," Phys. Rev. Lett. **86**(23), 5251–5254 (2001).
10. A. V. Nesterov and V. G. Niziev, "Laser beams with axially symmetric polarization," J. Phys. D. **33**(15), 1817–1822 (2000).
11. B. Tan and K. Venkatakrishnan, "A femtosecond laser-induced periodical surface structure on crystalline silicon," J. Micromech. Microeng. **16**(5), 1080–1085 (2006).

Optics EXPRESS

12. S. Gröblacher, T. Jennewein, A. Vaziri, G. Weihs, and A. Zeilinger, "Experimental quantum cryptography with qutrits," New J. Phys. **8**(5), 75 (2006).
13. G. Machavariani, S. Jackel, Y. Lumer, I. Moshe, and A. Meir, "Spatially variable retardation plate for beam brightness enhancement in a high-power laser," Opt. Lett. **32**(17), 2626–2628 (2007).
14. I. Moshe, S. Jackel, and A. Meir, "Production of radially or azimuthally polarized beams in solid-state lasers and the elimination of thermally induced birefringence effects," Opt. Lett. **28**(10), 807–809 (2003).
15. C. Brunet, P. Vaity, Y. Messaddeq, S. LaRochelle, and L. A. Rusch, "Design, fabrication and validation of an OAM fiber supporting 36 states," Opt. Express **22**(21), 26117–26127 (2014).
16. Y. Yue, Y. Yan, N. Ahmed, J. Y. Yang, L. Zhang, Y. Ren, H. Huang, K. M. Birnbaum, B. I. Erkmen, S. Dolinar, M. Tur, and A. E. Willner, "Mode properties and propagation effects of optical orbital angular momentum (OAM) modes in a ring fiber," IEEE Photonics J. **4**(2), 535–543 (2012).
17. S. Li and J. Wang, "A compact trench-assisted multi-orbital-angular-momentum multi-ring fiber for ultrahigh-density space-division multiplexing (19 rings × 22 modes)," Sci. Rep. **4**(1), 3853 (2015).
18. X. M. Xi, G. K. L. Wong, M. H. Frosz, F. Babic, G. Ahmed, X. Jiang, T. G. Euser, and P. S. J. Russell, "Orbital-angular-momentum-preserving helical Bloch modes in twisted photonic crystal fiber," Optica **1**(3), 165–169 (2014).
19. S. Ramachandran and P. Kristensen, "Optical vortices in fiber," Nanophotonics **2**(5–6), 455–474 (2013).
20. S. Ramachandran, P. Kristensen, and M. F. Yan, "Generation and propagation of radially polarized beams in optical fibers," Opt. Lett. **34**(16), 2525–2527 (2009).
21. S. Piehler, X. Délen, M. Rumpel, J. Didierjean, N. Aubry, T. Graf, F. Balembois, P. Georges, and M. A. Ahmed, "Amplification of cylindrically polarized laser beams in single crystal fiber amplifiers," Opt. Express **21**(9), 11376–11381 (2013).
22. M. Fridman, M. Nixon, M. Dubinskii, A. A. Friesem, and N. Davidson, "Fiber amplification of radially and azimuthally polarized laser light," Opt. Lett. **35**(9), 1332–1334 (2010).
23. N. Bozinovic, Y. Yue, Y. Ren, M. Tur, P. Kristensen, H. Huang, A. E. Willner, and S. Ramachandran, "Terabit-scale orbital angular momentum mode division multiplexing in fibers," Science **340**(6140), 1545–1548 (2013).
24. M. Gu, H. Kang, and X. Li, "Breaking the diffraction-limited resolution barrier in fiber-optical two-photon fluorescence endoscopy by an azimuthally-polarized beam," Sci. Rep. **4**(1), 3627 (2015).
25. J. Demas, M. D. W. Grogan, T. Alkeskjold, and S. Ramachandran, "Sensing with optical vortices in photonic-crystal fibers," Opt. Lett. **37**(18), 3768–3770 (2012).
26. L. Yan, E. Auksorius, N. Bozinovic, G. J. Tearney, and S. Ramachandran, "Optical fiber vortices for STED nanoscopy," in CLEO: 2013 (Optical Society of America, San Jose, California, 2013), p. CTu3N.2.
27. H. Ji, Y. Ruan, S. A. Vahid, H. Ebendorff-Heidepriem, and T. M. Monro, "Suspended core fibers for the transmission of cylindrical vector modes," J. Lit. Technol. **34**(24), 5620–5626 (2016).
28. J. R. Moffitt, C. Osseforth, and J. Michaelis, "Time-gating improves the spatial resolution of STED microscopy," Opt. Express **19**(5), 4242–4254 (2011).
29. H. Ebendorff-Heidepriem, S. C. Warren-Smith, and T. M. Monro, "Suspended nanowires: fabrication, design and characterization of fibers with nanoscale cores," Opt. Express **17**(4), 2646–2657 (2009).
30. Y. Ruan, E. P. Schartner, H. Ebendorff-Heidepriem, P. Hoffmann, and T. M. Monro, "Detection of quantum-dot labelled proteins using soft glass microstructured optical fibers," Opt. Express **15**(26), 17819–17826 (2007).
31. E. Rittweger, K. Y. Han, S. E. Irvine, C. Eggeling, and S. W. Hell, "STED microscopy reveals crystal colour centres with nanometric resolution," Nat. Photonics **3**(3), 144–147 (2009).
32. V. Westphal and S. W. Hell, "Nanoscale resolution in the focal plane of an optical microscope," Phys. Rev. Lett. **94**(14), 143903 (2005).
33. H. Ebendorff-Heidepriem and T. M. Monro, "Extrusion of complex preforms for microstructured optical fibers," Opt. Express **15**(23), 15086–15092 (2007).
34. S. Afshar V, S. C. Warren-Smith, and T. M. Monro, "Enhancement of fluorescence-based sensing using microstructured optical fibres," Opt. Express **15**(26), 17891–17901 (2007).
35. H. Ebendorff-Heidepriem, Y. Li, and T. Monro, "Reduced loss in extruded soft glass microstructured fibre," in COIN-ACOFT 2007 - Joint International Conference on the Optical Internet and the 32nd Australian Conference on Optical Fibre Technology(2007), p. 1–3.
36. S. Ramachandran, J. M. Fini, M. Mermelstein, J. W. Nicholson, S. Ghalmi, and M. F. Yan, "Ultra-large effective-area, higher-order mode fibers: a new strategy for high-power lasers," Laser Photonics Rev. **2**(6), 429–448 (2008).
37. E. Collett, *Polarized light: fundamentals and applications* (Marcel Dekker, Inc., 1993).
38. L. Yan, P. Gregg, E. Karimi, A. Rubano, L. Marrucci, R. Boyd, and S. Ramachandran, "Q-plate enabled spectrally diverse orbital-angular-momentum conversion for stimulated emission depletion microscopy," Optica **2**(10), 900–903 (2015).
39. B. Neupane, F. Chen, W. Sun, D. T. Chiu, and G. Wang, "Tuning donut profile for spatial resolution in stimulated emission depletion microscopy," Rev. Sci. Instrum. **84**(4), 043701 (2013).